Nano World Journal

https://doi.org/10.17756/nwj.2024-s1-005

Research Article

Open Access

Exploring Transparent ZnO-based Memristors: Synaptic Emulation and Conduction Mechanism with Varied Top Electrodes

P. Hajara, P. Praveen, T. Priya Rose and K.J. Saji*

International School of Photonics, Cochin University of Science and Technology, Kochi, Kerala, India

***Correspondence to:**
K.J. Saji
International School of Photonics,
Cochin University of Science and Technology,
Kochi, Kerala, India.
E-mail: saji@cusat.ac.in

Received: January 03, 2024
Accepted: March 05, 2024
Published: March 08, 2024

Citation: Hajara P, Praveen P, Rose TP, Saji KJ. 2024. Exploring Transparent ZnO-based Memristors: Synaptic Emulation and Conduction Mechanism with Varied Top Electrodes. *NanoWorld J* 10(S1): S19-S25.

Published by United Scientific Group

Abstract

Memristors are a new class of devices that can replace integrated electronic devices in applications involving sophisticated computing, digital and analog circuits, and neuromorphic networks. In this work, we report a transparent synaptic memristor with the nano-device structure indium tin oxide/zinc oxide/indium tin oxide (ITO/ZnO/ITO) that exhibits potentiation and depression behavior resembling the brain's synapses. The layers of ZnO and ITO were deposited by radio frequency (RF) magnetron sputtering. Nano-dimension of the sandwiched layer results in high electric field intensity between the electrodes even at small potentials and facilitates the migration of ions. This synaptic device has spike-dependent synaptic plasticity and paired-pulse facilitation/depression. This study reveals that the synaptic weight changes are more prominent when wider pulses or shorter-interval pulses are applied. The switching behavior of the ZnO-based memristor is studied by altering the top electrodes. Devices with top electrodes made of ITO and silver (Ag) demonstrated bipolar, forming free and filament-type resistive switching. Interface-type resistive switching was observed in a device with gold (Au) as the top electrode (Au/ZnO/ITO). The conduction mechanics of these memristors were also investigated.

Keywords

Indium tin oxide layer, Zinc oxide, Nano-dimension, Memristors

Introduction

Developing artificial intelligence systems that are capable of carrying out complicated activities is a major technological aim for many nations because it could have a huge social impact. Neuromorphic computing has been proposed as a potential solution to process and store information and it is anticipated that the artificial synapses-based neuromorphic computing system will represent the next generation with exceptional parallel processing capability and processing speed. Various artificial synapses have been created, and among them, the memristor is a non-volatile memory technology that can simulate the typical brain synaptic response [1-3]. This device can switch between several resistive states in response to suitable voltage stimuli. Memristors typically have a top electrode, functional layer, and bottom electrode, similar to the presynaptic neuron, synaptic cleft, and postsynaptic neuron of a biological synapse. Before employing the device to physically duplicate synapses, we must evaluate their synaptic plasticity. Synaptic plasticity is the term used to describe the phenomena whereby variations in brain activity result in an increase or decrease in the efficiency of information transmission among neurons. The synaptic weight measures the intensity of signal transmission between synapses. The biological synapse must have adjustable synaptic weight and tunable resistance is its artificial counterpart [2]. The device resistance switches from a low resistance state (LRS or ON state) to a high resistance state (HRS or OFF state) and vice versa depending on the externally applied voltage. To exhibit synaptic properties in memristor, it's important to observe a gradual increase and decrease in the conductance state known as potentiation and depression, respectively [4]. Paired-pulse facilitation (PPF) or depression (PPD) and strike rate-dependent plasticity (SRDP) which can be imitated in resistive switching (RS)-based artificial synapses are other key properties of the biological synapse [4].

Materials that exhibit RS phenomena in resistive random-access memory include transition metal oxides, perovskite oxides, chalcogenides, and organic compounds [3-6]. Because of its great chemical stability, controllable electrical behaviour, and low-temperature manufacturing technique ZnO-based memristor is a material that has a lot of potential. Resistive memory is operated in either a unipolar or bipolar mode. In unipolar mode, the set and reset procedures occur in the same bias polarity, whereas in bipolar mode, they require different bias polarities [7]. These modes are affected by the material and microstructure of the nano-dimensional switching layer. The coexistence of bipolar and unipolar switching in ZnO-based devices was also demonstrated in earlier studies [8]. By altering the oxygen concentration during the ZnO deposition process, it is possible to build devices that demonstrate switching behavior from unipolar to bipolar. Many efforts have been made to create a generalized physical model that can explain RS phenomena in ZnO-like metal oxide thin films and the conducting filament model is widely accepted [3, 8]. The fundamental idea behind the filamentary conducting theory is that the metal oxides typically contain several electrically active defects, such as oxygen vacancies, and the mobility of these defects generates switching behavior. However, an excessive defect concentration causes a lot of leakage current and deteriorates the performance of the device [9]. Therefore, to create high-quality films with fewer native defects, controlled ZnO film growth is necessary. Additionally, the fabrication of highly resistant ZnO film may open the prospect of thinning down the switching layer and lowering the operating power [10]. ZnO-based memristors have been developed experimentally in various studies, revealing the features of a synaptic system [4, 10, 11]. However, more studies are needed to explore the conduction mechanism and synaptic behavior of ZnO-based memristors.

The growth of conducting filaments in the ZnO-based memristor nano-device is affected by several variables. The top metal electrode of the device can have a significant impact on its current-voltage (I-V) behavior [12]. It has been demonstrated that the forming, set, and reset voltages, HRS, and LRS values, are all correlated with the top electrode material [13, 14]. In addition to electrodes, the microstructure and defects of the ZnO film significantly impact switching behavior. Extended defects like grain boundaries and dislocations may offer easy diffusion pathways for metallic ions and oxygen vacancies [15]. In the present study, we fabricated an ITO/ZnO/ITO-based transparent memristor for neuromorphic application and demonstrated various synaptic properties like potentiation, depression, PPF, PPD, and SRDP. The switching behavior of the ZnO-based memristor is examined by altering the top electrodes. A study of the conduction mechanism of these devices was also done.

Experimentation

RF magnetron sputtering was used to create a 65 nm thick ZnO film with a ZnO target on the commercially available transparent ITO-coated glass substrate. For this, the chamber was emptied to a base pressure of around 2 x 10^{-6} mbar. The working pressure was held at 6 x 10^{-3} mbar, and the ratio of Ar/O_2 gas flow was 5:4 throughout the sputtering process. Sputtering time and power were 30 min and 70 W, respectively. The substrate and target were separated by 10 cm. To fabricate an ITO/ZnO/ITO nano-device, ITO (top electrode) was sputtered on an ITO/ZnO structure from an ITO target using a 500 µm shadow mask. The power of sputtering was 100 W, and the flow rate of Ar gas was 10 sccm. A thickness of about 510 nm was attained after an hour of sputtering. ITO/ZnO/Ag and ITO/ZnO/Au devices were fabricated by evaporating Ag or Au on the ITO/ZnO structure.

The structural characteristics of ZnO thin films were examined using X-ray diffraction (XRD; Bruker Kappa Apex II). Transmission spectra were recorded by a JASCO V-770 spectrophotometer and the optical bandgap of ZnO thin film was determined through a Tauc plot. Field emission-scanning electron microscopy (FE-SEM) was used to examine the surface and cross-sectional morphologies (Zeiss Sigma HV). An X-ray photoelectron spectroscopy (XPS) study was done to examine the oxygen vacancies in the ZnO film (Thermo Scientific™ ESCALAB™ Xi+). A probe station and Keithley 2614B SMU, coded in LabView, were used to perform electrical characterizations of the nano-devices. A voltage bias was applied on the top electrode while grounding the bottom electrode.

Results and Discussion

Figure 1a represents the XRD pattern of the ZnO thin film deposited on a glass slide through RF magnetron sputtering. Only one peak, (002), was seen in the patterns, which is compatible with a ZnO wurtzite hexagonal structure. This diffraction peak at 2θ = 33.6° reveals the C-axis-oriented growth of the film. Figure 1b depicts the FE-SEM image of the same and shows homogeneous and densely packed film growth. Figure 1c displays the Tauc plot of the ZnO thin film

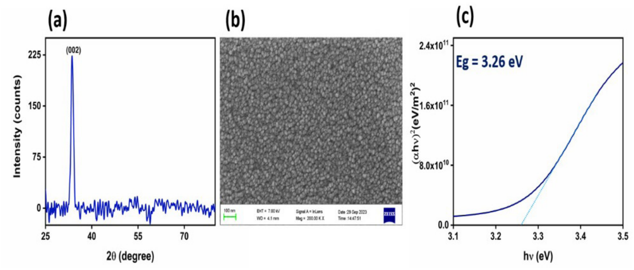

Figure 1: (a) XRD pattern and **(b)** FE-SEM image of the ZnO thin films deposited on glass through RF magnetron sputtering. XRD pattern reveals the wurtzite crystal structure and FE-SEM shows ZnO's homogeneous and densely packed growth. **(c)** Tauc plot for the ZnO thin film estimated from transmission spectra.

calculated from the transmission spectra, and the bandgap value is determined to be 3.26 eV.

The metal-insulator-metal arrangement is typically used to investigate the possible existence of RS phenomena in metal oxide thin films like ZnO [8, 11]. Figure 2a depicts the ITO/ZnO/ITO-based memristor nano-device structure, where the sputtered ZnO, of thickness in nanometers, serves as the switching layer, and ITO layers serve as the bottom (BE) and top electrode (TE). Each layer of this ITO/ZnO/ITO device is visible in the cross-section FE-SEM as seen in figure 2b. The thickness of the deposited layers of ITO (BE), ZnO, and ITO (TE) are found to be around 170 nm, 65 nm, and 510 nm, respectively. The transmission spectra of the device along with ZnO layer transparency are shown in figure 2c which reveals the high transparency of the device in the visible region. The inset shows the photograph of the fabricated transparent ITO/ZnO/ITO device. The multilayer coatings are responsible for the fringes in the transmittance spectra that appear after 460 nm. To study the switching properties of the memristive device, I-V measurement was done by applying a bias voltage to the top ITO (TE), while the BE was grounded. The device shows bipolar switching characteristics as shown in figure 2d. The nano-device switches from HRS to LRS as the voltage is swept from 0 to 2 V and flips back from LRS to HRS when negative voltage is applied. A current compliance of 20 μA was used to prevent the breakdown of the device.

A few models have been proposed for the switching behavior of the ZnO-based memristor. The two main methods found in the various filamentary-based RS devices are valence change mechanism (VCM) and electrochemical metallization (ECM) [16, 17]. In VCM, oxygen vacancies (anions) move in the active layer to create a conductive filament (CF). On the other hand, in the case of ECM, positively charged metal cations from the active top electrode move to the cathode surface and create the CF. The RS behavior in ITO/ZnO/ITO artificial synapses has been suggested to be caused by oxygen vacancy migration and recombination (recombination of oxygen vacancies with non-lattice oxygen ions), which makes or breaks the CF (shown in figures 3a and 3b) [11].

Since it is well known that the oxygen vacancy (V_o) plays a significant role in the switching mechanism of memristor devices, XPS spectra of the O1s core level were examined to determine the oxygen vacancy concentration in the ZnO films. The individual O1s peak has been deconvoluted to produce the five unique Lorentzian Gaussian curves centered at binding energies 530.12, 531.01, 531.88, 532.67, and 533.88 eV (Figure 3c). O atoms at the regular lattice site (O_L) are the source of the low binding energy curve at 530.12 eV [18]. The existence of O vacancies is responsible for the medium binding energy curve at 531.01 eV. Generally, a forming voltage is essential for the metal oxide memristor devices, and it is reported that non-lattice oxygen ions and pre-existing oxygen vacancies in the ZnO layer are largely responsible for forming free RS [18, 19]. Due to the oxygen vacancies that are already present in the ZnO film, a high voltage forming process is not necessary in our device. Forming-free devices have more stable RS characteristics and prevent electrode damage in contrast to forming-necessary cells [20]. Interstitial O atoms (O_I), or non-stoichiometric oxygen, are responsible for the highest binding energy curve, which is measured at 531.88 eV. The peaks at 532.67 and 533.88 eV are associated with oxygen species that have been adsorbed, such as O_2 and H_2O, on the surface of ZnO. The XPS spectra corresponding to the Zn atom in ZnO are depicted in figure 3d. Zn atoms at regular lattice positions in ZnO bulk are responsible for the peaks of the Zn $2p_{3/2}$ and Zn $2p_{1/2}$ levels, which correspond to binding energies at 1021.66 and 1044.68 eV, respectively [21]. The binding energy difference of 23.02 eV demonstrates that Zn atoms are fully oxidized and agree with previously published Zn2p values [18, 21]. This suggests there are no free metallic zinc ions, which rules out the possibility of any

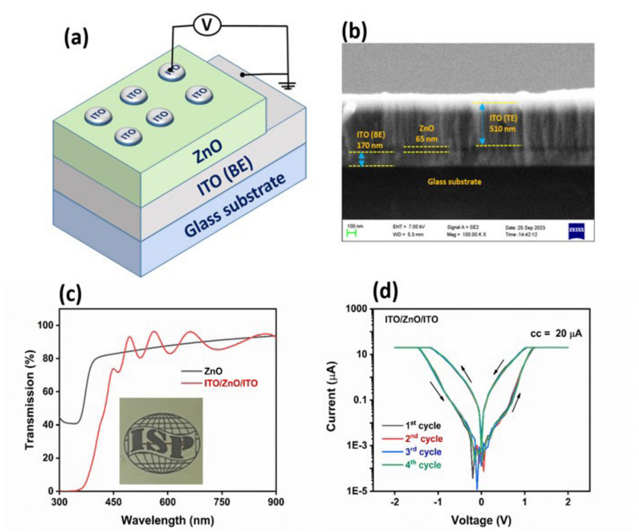

Figure 2: (a) Schematic illustration of ITO/ZnO/ITO-based memristor, **(b)** Cross-section FESEM image of the fabricated device, **(c)** Transmission spectra of the device along with transparency of ZnO, and **(d)** I-V properties of fabricated ITO/ZnO/ITO memristor. To avoid device breakdown, a current compliance of 20 μA was used.

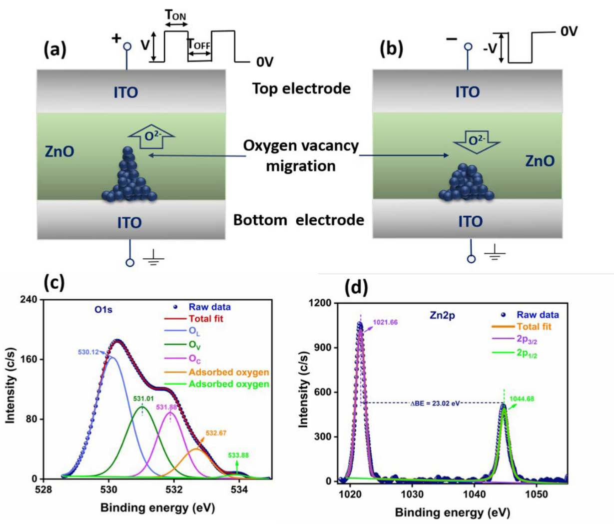

Figure 3: Schematic illustration of **(a)** the development of CFs for positive input pulses caused by oxygen vacancy migration and **(b)** filament rupturing due to oxygen vacancy migration in the opposing direction. The XPS spectra of **(c)** O1s core levels and **(d)** Zn2p levels in the ZnO active layer.

metallic ion conduction in the ZnO layer.

The synapse, which connects neurons in the human brain, allows them to communicate with one another (see figure 4a). The presynaptic neurons are made up of synaptic vesicles that contain neurotransmitters and postsynaptic neurons are made up of receptors. When an action potential occurs on the presynaptic neuron, the synaptic vesicles release neurotransmitters (Na^+ or Ca^{2+} ions) into the synaptic cleft and strengthen the link between presynaptic and postsynaptic neurons. This depends on the timing and amplitude of the action potential. Similar to this, in ITO/ZnO/ITO artificial synapses, the connection between BE and TE strengthens when oxygen vacancies or ions move across the ZnO matrix to form CF [22]. TE, an active layer, and BE of the devices are comparable to presynaptic neurons, synaptic cleft, and postsynaptic neurons, respectively. The filaments begin to expand gradually in response to positive electrical pulses resulting in a potentiation behavior; in contrast, the filament begins to rupture gradually in response to negative electrical pulses; this behavior is known as depression [23]. The fabricated ITO/ZnO/ITO artificial synapse exhibit potentiation when 200 continuous positive input stimuli with amplitudes of 0.9 V, T_{ON} of 100 ms, and T_{OFF} of 100 ms are applied (Figure 4b). By the application of this positive pulse, the filament grows from the BE and increases the conductivity of the device. When a train of negative pulses (amplitude = -0.9 V, T_{ON} = 100 ms, T_{OFF} = 100 ms) is applied the filament starts to migrate reversely decreasing the conductivity and leading to the depression of synaptic weight.

Synaptic plasticity, which comprises short-term plasticity (STP) and long-term plasticity (LTP), is the most significant feature of the biological synapse. STP is characterized by physiological processes known as PPF and PPD, in which a preceding stimulus changes the subsequent synaptic responses [24]. These characteristics of the constructed device are examined by stimulating with a pulse pair with varying pulse intervals while maintaining a constant pulse width. The artificial synapse's PPF (PPD) % is defined as follows [25].

$$PPF\left(PPD\right)(\%) = \frac{\left(I_2 - I_1\right)}{I_1}100\% \tag{1}$$

Where I_1 and I_2 are, respectively, the postsynaptic currents resulting from the first and second pulses.

Five separate pulse pairs with various pulse intervals (from 200 ms to 600 ms) are used to calculate PPF and PPD%. The PPF index, which symbolizes the temporal potentiation effect, is shown to decrease with pulse interval exhibiting an exponential decay as shown in figure 5a. The temporal depression effect is demonstrated by the PPD (Figure 5b), which is seen to increase exponentially with pulse interval. The PPF (PPD) curve can be modeled using the following double exponential decay function [25].

$$PPF\left(PPD\right)(\%) = A_1 \exp\left(\frac{-t}{\tau_1}\right) + A_2 \exp\left(\frac{-t}{\tau_2}\right) \tag{2}$$

Where t is the pulse interval, A_1 and A_2 are the initial facilitation percentages, and τ_1 and τ_2 are the corresponding relaxation periods for rapid and slow decay terms.

The fitted curve for PPF yields the parameters τ_1 = 25 ms, and τ_1 = 392 ms, and the parameters obtained from the fitted PPD curves are τ_1 = 74 ms, and τ_2 = 599 ms. The values of relaxation times τ_1 and τ_2 are consistent with those of biological synapses (relaxation times τ_1 are in the tens of milliseconds and relaxation times τ_2 are in the hundreds of milliseconds) [25].

By applying pulses with various widths (T_{ON}) and intervals (T_{OFF}), which provide the temporal correlation between spike signals and synaptic weight, the SRDP of the device was examined. First, synaptic weight dependency on T_{ON} is assessed by keeping the T_{OFF} (100 ms) and pulse amplitude (0.9 V) constant (Figure 5c). As T_{ON} increases, the time gets to migrate the oxygen vacancy is more for each pulse, and thicker filaments are formed. This increases the rate of change of conductivity with T_{ON} [26]. Figure 5d depicts the effect of synaptic rate on T_{OFF} keeping T_{ON} (100 ms) and amplitude (0.9 V) constant. A considerable increase in current is shown in response to pulses with lower T_{OFF}. The reason for this phenomenon is that tiny T_{OFF} does not provide the device enough time for spontaneous decay as the preceding pulse follows quickly [26]. On the other hand, the device receives sufficient time for spontaneous decay at a higher T_{OFF}, and the rate of change of resistance is minimal.

The TE-dependent I-V curves of the ZnO-based memristor are studied by changing TEs as ITO, Ag, and Au as seen in figure 6a, 6b, and 6c. The switching mechanisms are very dependable on the TE. ITO/ZnO/Ag device also shows the bipolar switching as an ITO/ZnO/ITO device (Figure 6a and 6b). A threshold-type switching was observed in the device with an Au TE as depicted in figure 6c and the interface effect between the Au TE and ZnO/ITO is responsible for this [27]. Moreover, this device displayed a higher set voltage than Ag, which may be due to the low oxygen affinity of Au to Ag. Ag TE has a high oxygen affinity, so oxygen ions migrate towards it when bias is applied. This causes oxygen vacancies to occur in the device oxide layer, which eventually brings them together to form a CF. Depending on the TE, the devices' reset behavior reveals changes in the I-V curve. With an ITO

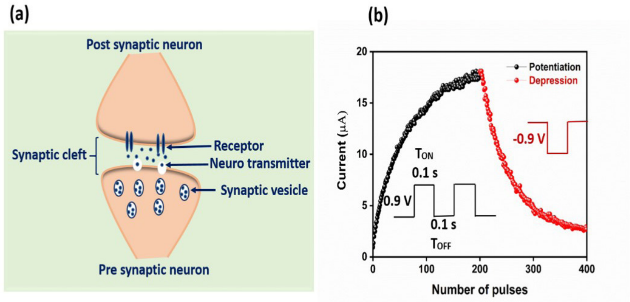

Figure 4: (a) A biological synapse is shown schematically. The link between the presynaptic and postsynaptic neurons is strengthened when an action potential activates on the presynaptic neuron, releasing neurotransmitters into the synaptic cleft and attracting them to receptors. **(b)** Potentiation and depression of the artificial synapse ITO/ZnO/ITO for positive and negative input pulses, respectively.

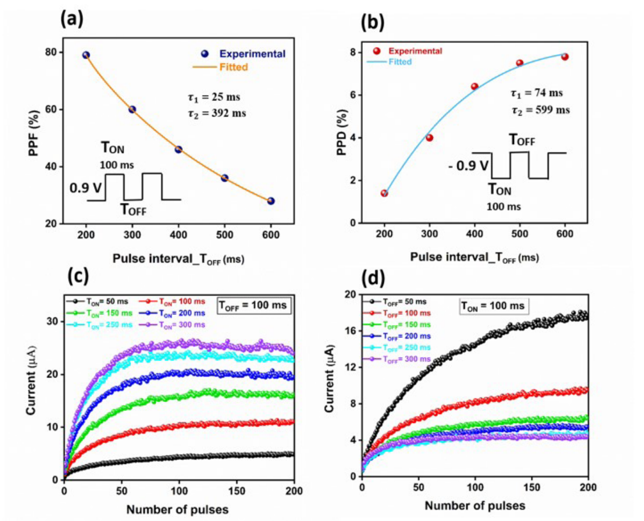

Figure 5: ITO/ZnO/ITO synapse displaying PPF and PPD. **(a)** The percentage PPF is plotted vs pulse interval; the curve is fitted with equation 2, **(b)** The percentage of PPD vs pulse interval with fitting parameters, **(c)** Synaptic weight dependency on T_{ON} at constant T_{OFF} (100 ms) and amplitude (0.9 V), and **(d)** Synaptic weight dependency on T_{OFF} with constant T_{ON} (100 ms) and amplitude (0.9 V).

TE, symmetrical I-V behavior is seen on both polarities. On the other hand, a device with Ag as the TE resets in a different way. Ag ions are known to be more diffusible into the ZnO layer because of their tiny ionic sizes and low electronegativity values, and the ECM model helps to explain this [28]. In contrast to VCM devices, the use of active anodes facilitates the creation and rupture of CF, and therefore the set and reset voltages in the ECM are lower than those in the VCM. But in our case, such a shift in set voltage is not seen. Therefore, we can conclude that oxygen migration is primarily responsible for the switching in ITO/ZnO/Ag devices. However, there is a chance that the Ag will migrate, and this may affect the reset process.

The conduction mechanisms of ITO/ZnO/ITO, ITO/ZnO/Ag, and ITO/ZnO/Au devices were studied by analyzing a double logarithmic plot of positive bias region as shown in figure 6d, 6e, and 6f. The slope of the first two devices is 1.1 (I α V) at the low voltage region of HRS suggesting the conduction mechanism is purely ohmic. This ohmic conduction process in the low-voltage domain is consistent with earlier research [29]. The nonlinear effects are observed at higher voltage regions and a sudden increase in current is observed which denotes the trap unfilled space charge limited conduction (SCLC) which follows child's law (I α V^2) [30]. A further increase in bias (higher than 0.9 V) causes trap states to fill up and follow trap-filled space charge limited conduction (where I α V^α and α >2). According to the results of the I-V curve fitting of the devices' set process, it can be concluded that the electrical conduction that governs switching in the devices adheres to the trap-controlled SCLC model, which is a common filamentary formation and dissolution model [30, 31]. In the HRS region of the ITO/ZnO/Ag device, ohmic conduction is predominant. Whereas in the ITO/ZnO/ITO device, the low voltage region follows ohmic conduction and nonlinearity observed in the high voltage region. This nonlinearity is attributed to the high resistance condition seen at the interface of ZnO and ITO (TE) [32]. It may be due to the oxygen-rich layer exhibited at the TE interface due to the migration of oxygen from ITO to the vacancies of the ZnO layer. This behaves as a series resistance at the interface and prevents continuous filament formation. It is predicted that the ITO electrode serves as an oxygen reservoir and can provide enough non-lattice oxygen ions to fill the oxygen vacancies into the active layer [18]. The SCLC equation is unable to fit the I-V curve of the ITO/ZnO/Au device at a high voltage region (see inset of figure 6f) indicating a separate current conduction mechanism. The current drastically fluctuates in the low-voltage region. The electrodes with various work-functions provide different built-in internal potentials and the band alignment between the switching ZnO layer and the metal electrodes affects the interface resistance, current level, switching power, and conduction mechanism of the devices [33]. A corresponding change in the I-V curve and conduction mechanism is observed by various TEs (ITO, Ag, and Au). As seen in figure 6f, there is a linear relationship between ln(I) and Sqrt(V) for ITO/ZnO/Au device. This linear fitting suggests that Schottky emission dominates the current conduction at higher voltage region of HRS, a commonly found conduction mechanism in dielectric film [13, 34].

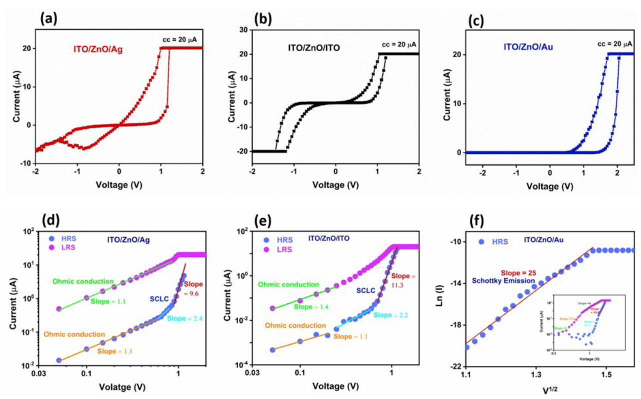

Figure 6: I-V curve for the **(a)** ITO/ZnO/ITO, **(b)** ITO/ZnO/Ag, and **(c)** ITO/ZnO/Au memristor devices. The I-V behavior depends on the TE of the device. Conduction mechanism for **(d)** ITO/ZnO/ITO and **(e)** ITO/ZnO/Ag and **(f)** ITO/ZnO/Au device. In HRS, the first two devices display ohmic conduction followed by SCLC. In LRS, ohmic conduction is observed in the device with ITO as the TE while a nonlinear curve is observed in the high-voltage region of the device with Ag as the TE. In the ITO/ZnO/Au device the conduction is governed by the Schottky conduction mechanism.

Conclusion

An ITO/ZnO/ITO-based transparent and forming free memristor was fabricated by RF magnetron sputtering. Synaptic behavior of the nano-device such as potentiation, depression, PPF, PPD, and SRDP was demonstrated. This study shows that pulses with higher widths or shorter intervals are more effective at enhancing synaptic weight alterations. The switching behavior of the ZnO-based memristor is investigated by changing the TEs. ITO and Ag show a forming free and bipolar RS behavior. The Au/ZnO/ITO device demonstrated a threshold-type switching attributed to the interface effect between the Au TE and the

ZnO switching layer. Additionally, the conduction mechanism of the nano-devices was examined. While the low voltage region of the HRS displayed ohmic behavior, the high voltage portion of the HRS was well suited to the SCLC model for the devices with Ag and ITO. When ITO is used as the TE, a nonlinear curve is seen in contrast to the ohmic behavior of an ITO/ZnO/Ag device in the high voltage region of the LRS curve which may be due to the high resistance interface near the top electrode. Whereas the ITO/ZnO/Au device shows a Schottky conduction in the HRS region. Different TEs (ITO, Ag, and Au) show a corresponding variation in the I-V curve and the conduction mechanism which may be due to the variation in the work function and electronegativity of the electrode material.

Acknowledgments

For the NREF Fellowship, Hajara thanks the Ministry of New and Renewable Energy (MNRE). The Kerala government provided us with financial support through the PLEASE initiative, and we would like to express our gratitude. Furthermore, we acknowledge the financial assistance provided by DST-PURSE to purchase the RF magnetron sputtering system.

Conflict of Interest

None.

References

1. Park Y, Lee JS. 2017. Artificial synapses with short-and long-term memory for spiking neural networks based on renewable materials. *ACS Nano* 11(9): 8962-8969. https://doi.org/10.1021/acsnano.7b03347
2. Choi S, Yang J, Wang G. 2020. Emerging memristive artificial synapses and neurons for energy-efficient neuromorphic computing. *Adv Mater* 32(51): 2004659. https://doi.org/10.1002/adma.202004659
3. Zhang L, Tang Z, Yao D, Fan Z, Hu S, et al. 2022. Synaptic behaviors in flexible Au/WOx/Pt/mica memristor for neuromorphic computing system. *Mater Today Phys* 23: 100650. https://doi.org/10.1016/j.mtphys.2022.100650
4. Chen W, Song L, Wang S, Zhang Z, Wang G, et al. 2023. Essential characteristics of memristors for neuromorphic computing. *Adv Electron Mater* 9(2): 2200833. https://doi.org/10.1002/aelm.202200833
5. Sahoo S, Prabaharan SR. 2017. Nano-ionic solid state resistive memories (re-RAM): a review. *J Nanosci Nanotechnol* 17(1): 72-86. https://doi.org/10.1166/jnn.2017.12805
6. Xu W, Cho H, Kim YH, Kim YT, Wolf C, et al. 2016. Organometal halide perovskite artificial synapses. *Adv Mater* 28(28): 5916-5922. https://doi.org/10.1002/adma.201506363
7. Khan R, Ilyas N, Shamim MZM, Khan MI, Sohail M, et al. 2021. Oxide-based resistive switching-based devices: fabrication, influence parameters and applications. *J Mater Chem C* 9(44): 15755-15788. https://doi.org/10.1039/d1tc03420k
8. Lee S, Kim H, Park J, Yong K. 2010. Coexistence of unipolar and bipolar resistive switching characteristics in ZnO thin films. *J Appl Phys* 108(7): 076101. https://doi.org/10.1063/1.3489882
9. Simanjuntak FM, Prasad OK, Panda D, Lin CA, Tsai TL, et al. 2016. Impacts of Co doping on ZnO transparent switching memory device characteristics. *Appl Phys Lett* 108(18): 183506. https://doi.org/10.1063/1.4948598
10. Zhao H, Dong Z, Tian H, DiMarzi D, Han MG, et al. 2017. Atomically thin femtojoule memristive device. *Adv Mater* 29(47): 1703232. https://doi.org/10.1002/adma.201703232
11. Subin PS, Saji KJ, Jayaraj MK. 2021. Plasticity and learning behavior emulated in a ZnO based transparent artificial synapse. *Thin Solid Films* 737: 138924. https://doi.org/10.1016/j.tsf.2021.138924
12. Peng HY, Li GP, Ye JY, Wei ZP, Zhang Z, et al. 2010. Electrode dependence of resistive switching in Mn-doped ZnO: filamentary versus interfacial mechanisms. *Appl Phys Lett* 96(19): 192113. https://doi.org/10.1063/1.3428365
13. Praveen P, Rose TP, Saji KJ. 2022. Top electrode dependent resistive switching in M/ZnO/ITO memristors, M = Al, ITO, Cu, and Au. *Microelectron J* 121: 105388. https://doi.org/10.1016/j.mejo.2022.105388
14. Xue WH, Xiao W, Shang J, Chen XX, Zhu XJ, et al. 2014. Intrinsic and interfacial effect of electrode metals on the resistive switching behaviors of zinc oxide films. *Nanotechnology* 25(42): 425204. https://doi.org/10.1088/0957-4484/25/42/425204
15. Huang HW, Kang CF, Lai FI, He JH, Lin SJ, et al. 2013. Stability scheme of ZnO-thin film resistive switching memory: influence of defects by controllable oxygen pressure ratio. *Nanoscale Res Lett* 8: 483. https://doi.org/10.1186/1556-276X-8-483
16. Huang CH, Huang JS, Lai CC, Huang HW, Lin SJ, et al. 2013. Manipulated transformation of filamentary and homogeneous resistive switching on ZnO thin film memristor with controllable multistate. *ACS Appl Mater Interfaces* 5(13): 6017-6023. https://doi.org/10.1021/am4007287
17. Xu R, Jang H, Lee MH, Amanov D, Cho Y, et al. 2019. Vertical MoS_2 double-layer memristor with electrochemical metallization as an atomic-scale synapse with switching thresholds approaching 100 mV. *Nano Lett* 19(4): 2411-2417. https://doi.org/10.1021/acs.nanolett.8b05140
18. Kumar A, Das M, Garg V, Sengar BS, Htay MT, et al. 2017. Forming-free high-endurance Al/ZnO/Al memristor fabricated by dual ion beam sputtering. *Appl Phys Lett* 110(25): 253509. https://doi.org/10.1063/1.4989802
19. Mao Q, Ji Z, Xi J. 2010. Realization of forming-free ZnO-based resistive switching memory by controlling film thickness. *J Phys D Appl Phys* 43(39): 395104. https://doi.org/10.1088/0022-3727/43/39/395104
20. Huang Y, Shen Z, Wu Y, Wang X, Zhang S, et al. 2016. Amorphous ZnO based resistive random access memory. *RSC Adv* 6(22): 17867-17872. https://doi.org/10.1039/c5ra22728c
21. Pandey SK, Pandey SK, Mukherjee C, Mishra P, Gupta M, et al. 2013. Effect of growth temperature on structural, electrical and optical properties of dual ion beam sputtered ZnO thin films. *J Mater Sci Mater Electron* 24: 2541-2547. https://doi.org/10.1007/s10854-013-1130-5
22. Huang W, Xia X, Zhu C, Steichen P, Quan W, et al. 2021. Memristive artificial synapses for neuromorphic computing. *Nano Micro Lett* 13: 85. https://doi.org/10.1007/s40820-021-00618-2
23. Lisman J, Spruston N. 2005. Postsynaptic depolarization requirements for LTP and LTD: a critique of spike timing-dependent plasticity. *Nat Neurosci* 8(7): 839-841. https://doi.org/10.1038/nn0705-839
24. Wang TY, Meng JL, He ZY, Chen L, Zhu H, et al. 2019. Atomic layer deposited $Hf_{0.5}Zr_{0.5}O_2$-based flexible memristor with short/long-term synaptic plasticity. *Nanoscale Res Lett* 14: 102. https://doi.org/10.1186/s11671-019-2933-y
25. Zucker RS, Regehr WG. 2002. Short-term synaptic plasticity. *Annu Rev Physiol* 64(1): 355-405. https://doi.org/10.1146/annurev.physiol.64.092501.114547
26. Subin PS, Asha AS, Saji KJ, Jayaraj MK. 2021. Spike-dependent plasticity modulation in TiO_2-based synaptic device. *J Mater Sci Mater Electron* 32(10): 13051-13061. https://doi.org/10.1007/s10854-021-05710-2
27. Mainali P, Bastatas LD, Echeverria E, Wagle P, Sankaran P, et al. 2021. Addressing crosstalk in crossbar memory arrays with a resistive switching ZnO homojunction diode. *J Appl Phys* 129(20): 205106. https://doi.org/10.1063/5.0050564

28. Wu X, Cha D, Bosman M, Raghavan N, Migas DB, et al. 2013. Intrinsic nanofilamentation in resistive switching. *J Appl Phys* 113(11): 114503. https://doi.org/10.1063/1.4794519
29. Guo T, Pan K, Jiao Y, Sun B, Du C, et al. 2022. Versatile memristor for memory and neuromorphic computing. *Nanoscale Horiz* 7(3): 299-310. https://doi.org/10.1039/d1nh00481f
30. Kim KM, Choi BJ, Shin YC, Choi S, Hwang CS. 2007. Anode-interface localized filamentary mechanism in resistive switching of TiO_2 thin films. *Appl Phys Lett* 91(1): 012907. https://doi.org/10.1063/1.2749846
31. Praveen P, Vijoy KV, John H, Saji KJ. 2022. Emulating synaptic plasticity with PDMS-Graphite composite memristor. *Mater Lett* 326: 132934. https://doi.org/10.1016/j.matlet.2022.132934
32. Maikap S, Jana D, Dutta M, Prakash A. 2014. Self-compliance RRAM characteristics using a novel $W/TaO_x/TiN$ structure. *Nanoscale Res Lett* 9: 292. https://doi.org/10.1186/1556-276X-9-292
33. Xue WH, Xiao W, Shang J, Chen XX, Zhu XJ, et al. 2014. Intrinsic and interfacial effect of electrode metals on the resistive switching behaviors of zinc oxide films. *Nanotechnology* 25(42): 425204. https://doi.org/10.1088/0957-4484/25/42/425204
34. Munjal S, Khare N. 2017. Valence change bipolar resistive switching accompanied with magnetization switching in $CoFe_2O_4$ thin film. *Sci Rep* 7(1): 12427. https://doi.org/10.1038/s41598-017-12579-x